

The Importance of Anisotropic Viscosity in Numerical Models, for Olivine Textures in Shear and Subduction Deformations

Yijun Wang *^{1,2}, Agnes Király ^{1,2}, Clinton P. Conrad ^{1,2}, Lars N. Hansen ³, Menno Fraters ⁴

¹Centre for Planetary Habitability (PHAB), University of Oslo, Oslo, Norway | ²Centre for Earth Evolution and Dynamics (CEED), University of Oslo, Oslo, Norway | ³Department of Earth and Environmental Sciences, University of Minnesota, Minneapolis, MN, USA | ⁴Department of Geological Sciences, University of Florida, Gainesville, FL, USA

Abstract Olivine lattice preferred orientation (LPO), or texture, forms in relation to deformation mechanisms such as dislocation creep and can be observed in the upper mantle as seismic anisotropy. Olivine is also mechanically anisotropic, meaning that it responds to stresses differently depending on the direction of the stress. Understanding the interplay between anisotropic viscosity (AV) and LPO, and their role in deformation, is necessary for relating seismic anisotropy to mantle flow patterns. In this study, we employ three methods to predict olivine texture (D-Rex, MDM, and MDM+AV) in a shear box model and a subduction model. D-Rex and MDM are two representative texture development methods that have been compared before, and our results are in line with previous studies showing that textures computed by D-Rex develop faster and are stronger and more point-like than textures calculated with MDM. MDM+AV uses the same isotropic mantle stresses and particle paths as D-Rex and MDM but includes the effect of AV for texture predictions. MDM+AV predicts a texture similar to MDM with a distinct girdle-like orientation for simple shear deformation or at low strain in the subduction model. At larger strains, MDM+AV's textures are more point-like and stronger compared to the other two methods. The effective viscosity for MDM+AV drops by up to 60% in a shear box model and can be either strengthened or weakened relative to isotropic viscosity for different regions of the subduction model experiencing different patterns of deformation. Our results emphasize the significant role of AV in olivine texture development, which could substantially affect geodynamic processes in the upper mantle.

Executive Editor:
Craig Magee
Associate Editor:
Maëlis Arnould
Technical Editor:
Mohamed Gouiza

Reviewers:
Lucan Mameri
Neil Ribe

Submitted:
25 August 2023
Accepted:
23 April 2024
Published:
2 May 2024

1 Introduction

Various geodynamic processes take place within Earth's upper mantle, such as subduction, seafloor spreading, lithospheric drips, and plumes, and have geological surface expressions such as tectonic plate movements, rifting, mountain building, volcanism, and dynamic topography. The physical and chemical properties of mantle materials exert major control over the deformation rates in the mantle associated with these processes. Understanding how minerals in the upper mantle respond to applied deformations is thus crucial for unraveling the mechanics of these geodynamic processes. Olivine, which constitutes approximately 60% of the upper mantle's composition, is the most abundant mineral, accompanied by pyroxene and other aluminous components. The olivine crystal structure has an orthorhombic crystal system characterized by three mutually perpendicular axes of different lengths ($a \equiv [100]$, $b \equiv [010]$, and $c \equiv [001]$). Slip primarily occurs

on the (010) and (001) planes, with corresponding slip directions along [100] and [001] (Table 1 in *Tommasi et al., 2000*). Deformation processes in the upper mantle, such as dislocation glide and dynamic recrystallization on specific slip systems, modify the lattice-preferred orientations (LPO), also known as crystal-preferred orientations (CPO), in olivine aggregates (*Falus et al., 2011; Hansen et al., 2014; Kaminski et al., 2004; Lee et al., 2002; Lopez-Sanchez et al., 2021*).

The LPO of olivine contributes significantly to macroscopic observations of seismic anisotropy. It is the primary source of seismic anisotropy in the upper mantle compared to extrinsic anisotropy resulting from mineral layering (*Hansen et al., 2021*). The widespread observations of seismic anisotropy around the world demonstrate that LPO is prevalent in the upper mantle (*Long and Becker, 2010; Long and Silver, 2009*). Therefore, investigating the microphysical mechanisms underlying seismic anisotropy in olivine is crucial for comprehending mantle dynamics and geodynamic processes.

*✉ yijun0509wang@gmail.com

Various numerical models have been developed to simulate olivine texture or LPO development and the resulting seismic anisotropy. These models can be categorized into three groups based on their assumptions: finite strain ellipsoid (FSE) models (McKenzie, 1979), polycrystal models (e.g., Molinari et al., 1987; Ribe and Yu, 1991; Sarma and Dawson, 1996), and director method models (Mühlhaus et al., 2002). FSE-based models consider texture as independent of the deformation path, relying only on the total finite strain to compute the LPO evolution (McKenzie, 1979). Polycrystal models track individual grains and their contributions to the overall LPO, incorporating the effect of the initial texture and past deformation. The viscoplastic self-consistent model (VPSC from Tommasi et al., 2000) and the dynamic-recrystallization induced LPO model (D-Rex from Kaminski et al., 2004), are two widely used models from this category. Both models were calibrated to fit experimental results and offer reasonable predictions of average LPO orientation and symmetry. Notably, VPSC requires relatively high computational resources (Hansen et al., 2021) and predicts both higher texture strength and larger anisotropy at high strains compared to experimental results (Hansen et al., 2016a). These challenges have been addressed by incorporating dynamic recrystallization into VPSC (Tommasi and Signorelli 2015) or by introducing pyramidal slip systems to accommodate strain while not generating rotation of the crystal lattice (Mameri et al., 2019). Mühlhaus et al. (2002) introduced the director method, where the normal vector to the easy-slip surface is defined as a director. The directors represent transverse isotropy and can be advected and rotated with the flow field to approximate 2-D LPO in numerical geodynamic models. Hansen et al. (2016a) introduced the modified director method (MDM), which separately describes grain rotations and mechanical responses to address 3-D LPO development at high strains. MDM improves computational efficiency and prediction accuracy for larger strains and complicated deformation paths. This computational efficiency allowed Hansen et al. (2016a) to numerically optimize the parameters in this model to best reproduce LPOs observed in their laboratory experiments. However, the application of MDM in subduction settings and other complex deformation scenarios remains unexplored.

Olivine also exhibits anisotropy in its mechanical properties including viscosity. Hansen et al. (2012) and Hansen et al. (2016b) conducted rock deformation experiments with olivine aggregates, and they demonstrated that the viscosity could change in response to the texture strength and orientation by approximately an order of magnitude, depending on the orientation of the principal stresses with respect to the texture alignment. While the above-mentioned texture evolution models have advanced our understanding of olivine LPO development, they have yet to incorporate the feedback effect of anisotropic

viscosity (AV) on deformation, which could influence deformation rates and ultimately impact mantle flow dynamics by accelerating or decelerating mantle flow. Previous numerical simulations demonstrated that AV can modify convection cells and patterns of the post-glacial rebound (Christensen, 1987; Han and Wahr, 1997), the temporal and spatial distributions of the Rayleigh-Taylor instabilities (Lev and Hager, 2008), and the flow field and thermal structure within the mantle wedges of subduction systems (Lev and Hager, 2011). More recent numerical modeling studies have shown that AV can significantly influence texture strength and orientation, which can increase or decrease effective viscosity by more than an order of magnitude. For instance, Blackman et al. (2017) found that LPO and AV development creates positive feedback in a mid-ocean ridge system, and the presence of AV significantly increases the calculated seismic anisotropy. Király et al. (2020) also predicted that olivine texture could weaken the asthenosphere and increase plate velocity by 60% if the plate movement is aligned with the preferred direction. AV related to olivine LPO has also been applied to lithospheric processes in VPSC models and (quasi) instantaneous numerical models based on VPSC to understand how LPO preserved in fossil mantle shear zones contributes to lithospheric fault reactivation (Mameri et al., 2019, 2020, 2023; Signorelli et al., 2021). However, further investigation is needed to compare different numerical methods for olivine texture computation and to assess the effects of AV induced by evolving LPO on texture predictions in both simple and complex settings.

In this study, we apply an extended version of the MDM method, which we call MDM+AV, for olivine texture prediction in a shear box setting and a subduction setting. MDM+AV combines the texture evolution model with a micromechanical model to incorporate the effect of AV. We follow an approach similar to that of Király et al. (2020), but use Hill's orthotropic yield criteria to model AV (Hill, 1948; Signorelli et al., 2021). Our goal is to explore different olivine texture prediction methods by comparing textures predicted by three different texture evolution models (specifically, D-Rex, MDM, and MDM+AV). We run geodynamic models using the software ASPECT (Bangerth et al., 2020; Heister et al., 2017; Kronbichler et al., 2012) and texture predictions are applied as a post-processing step with D-Rex implemented in ASPECT (Fraters and Billen, 2021), MDM, and MDM+AV. In particular, MDM+AV represents viscosity using an anisotropic viscosity tensor instead of a scalar. This allows us to study the effect of AV on texture prediction in both shear box and subduction settings without implementing AV directly within the geodynamic modelling tool. This work focuses on determining the effects of AV on olivine texture development and helps to determine whether implementing AV into future geodynamic modeling tools will significantly improve our understanding of geodynamic processes.

2 Methods

In this section, we present three distinct numerical approaches to modelling olivine LPO development. Previously, laboratory data on olivine deformation has been compared with several methods such as D-REX, VPSC, and the MDM (modified director method) models (Boneh et al., 2015; Boneh and Skemer, 2014; Hansen et al., 2016b,a; Mameri et al., 2019). Here we use D-REX and MDM, as well as MDM+AV, which is an extension of MDM in which the texture evolution model is coupled with a micromechanical model to include the role of anisotropic viscosity (AV) on LPO development. We test these three models in both a simple shear and a subduction setting. We run 3D geodynamic models of the shear box and subduction settings using ASPECT (Bangerth et al., 2020; Heister et al., 2017; Kronbichler et al., 2012) which utilizes D-Rex (Fraters and Billen, 2021) for texture prediction, while MDM and MDM+AV are applied as post-processors that do not influence the geodynamic model outcomes or the deformation path. ASPECT is an open-source, actively maintained geodynamic code integrated with Geodynamic World Builder (Fraters, 2020; Fraters et al., 2019), which allows us to create complex model setups such as the subduction model used in this study. In the following, we give details about the three applied methods as well as the geodynamic model setups for simple shear and subduction.

2.1 D-REX

D-Rex is a widely used polycrystal-type approach for predicting olivine texture evolution in aggregates subjected to large strains and high temperatures, particularly under intensive dynamic recrystallization (Kaminski and Ribe, 2001). It considers important factors such as the effect of initial LPO and deformation history, particularly relevant in the study of subduction systems where LPO can exhibit significant temporal and spatial variation. Compared to other polycrystal models like VPSC, D-Rex employs a simpler theory for olivine dynamic recrystallization and estimates dislocation density as a function of polycrystal orientation using only two free parameters. This simplification makes D-Rex less computationally intensive while still being constrained by numerous experimental observations. Kaminski et al. (2004) expanded the model by incorporating the enstatite phase and grain boundary migration into D-Rex.

In a recent work, Fraters and Billen (2021) implemented a version of D-Rex into the geodynamic modeling software ASPECT. Within ASPECT, D-Rex parameters are stored in particles, facilitating the tracking of olivine texture in regions of interest, such as around the subducting slab in the mantle. The textures predicted by D-Rex do not feed back into the deformation of the geodynamic model. D-Rex in ASPECT uses the criteria of Karato et al. (2008) to determine the olivine fabric type based on water

content and stress state, and the values of reference resolved shear stresses (RRSS) come from Table 1 in Kaminski and Ribe (2001) and Table 1 in Kaminski et al. (2004). While the evolution of volume fractions for olivine and enstatite are both possible in D-Rex, we only use olivine in our prediction of LPO and LPO-induced AV to be consistent with other methods (MDM and MDM+AV). The D-Rex parameters that we can manipulate in ASPECT are grain-boundary mobility (M_m), the threshold volume fraction for the activation of grain-boundary sliding (f_{gbs}), and the nucleation rate (λ) (Kaminski et al., 2004). Boneh et al. (2015) found that their experimental data exhibited a better fit with D-Rex using $M_m = 10$. Hansen et al. (2016a) also noted that D-Rex predictions with $M_m = 10$, $f_{gbs} = 0.4$, and $\lambda = 5$ were most comparable to results obtained using MDM and their laboratory experiments. In our model, we use $M_m = 10$ to avoid extreme grain growth on a few grains, which could lead to unrealistic textures.

2.2 MDM

Mühlhaus et al. (2002) introduced the director method and represented the anisotropy of a material by the orientation of the directors, which are the normal vectors of the layered planes or slip surfaces. The directors can be advected with the velocity field and will rotate under deformation. The evolution of LPO can be computed based on the relationship between the current deformation field represented by the velocity gradient tensor and the orientation of the directors.

In a subsequent study, Hansen et al. (2016a) modified the original director method by redefining the director as the Burger's vector and defining the rotation rate to be dependent on both the Burger's vector and the slip plane. In this manner, the different olivine slip systems together control grain rotation. They calibrated f^a , the relative rotation rate of each slip system (denoted by a) in the MDM texture evolution model, using samples deformed to different strains (Hansen et al., 2016a). For olivine, four slip systems can contribute to LPO development and grain rotation. Out of the four, the (010)[100] and (001)[100] slip systems have the highest relative rotation rates, while (010)[001] is the lowest, meaning that the latter is the strongest and contributes the least to grain rotation. The MDM method is applied as a post-processor on selected particles from simulations run in ASPECT. We store the temperature and velocity gradient history that a given particle experienced during the calculation. Using these and the particle's initial texture, we re-calculate the LPO development using the MDM model.

2.3 MDM+AV

To model texture evolution with the influence of AV, we combine the LPO development provided by the MDM model with the micromechanical model,

which has been calibrated with MDM to fit laboratory deformation experiments on olivine polycrystals (Hansen et al., 2016a). The micromechanical model uses a pseudo-Taylor approach, assuming that each grain of olivine experiences the same strain rate that is accommodated on three distinct slip systems, each with different resolved shear stress as described above for MDM (section 2.2). As for the MDM, the MDM+AV model is also applied as a post-processor on selected particles from the geodynamic model runs (see below in section 2.4). Using the stress and temperature history that a particle experienced during the run, we calculate new strain rates based on the anisotropic constitutive equation (e.g., Signorelli et al., 2021). The subsequent texture evolution is predicted with a velocity gradient ($D_{ij_anisotropy}$) that we obtain by scaling individual components of the velocity gradient that the particle experienced in the geodynamic model (D_{ij_model}) with the ratio between individual components of the anisotropic strain rate and the strain rate in the geodynamic model:

$$D_{ij_anisotropy} = D_{ij_model} \times \frac{\dot{\epsilon}_{ij_anisotropy}}{\dot{\epsilon}_{ij_model}}, \quad (1)$$

To calculate strain rates based on the viscous anisotropy of a given olivine LPO $\dot{\epsilon}_{ij_anisotropy}$, we have to find the six independent anisotropic viscosity parameters associated with the Hill yield criterion (Hill, 1948; Signorelli et al., 2021). Similarly to Király et al. (2020) and Signorelli et al. (2021), we apply the micromechanical model (Hansen et al., 2016a) multiple times on the given LPO to generate stresses associated with a number of different strain rates. By examining many of these pairs, we invert for the set of Hill's coefficients (F , G , H , L , M , and N from Hill, 1948) that minimizes the difference between the norm of the input strain rates for the micromechanical model and the norm of the strain rates ($\dot{\epsilon}$) calculated from the anisotropic constitutive equation (Signorelli et al., 2021):

$$\dot{\epsilon} = \gamma J(\sigma)^{n-1} \mathbf{A} : \mathbf{S}, \quad (2)$$

where γ is the temperature-dependent fluidity parameter defined in isotropic case as $\gamma = \gamma_0 \exp\left(\frac{-Q}{RT}\right)$, with the experimentally derived fluidity (γ_0), the activation energy (Q), the universal gas constant (R), and the temperature (T). $J(\sigma)$ is the equivalent stress defined by the Hill yield criteria (Hill, 1948):

$$J(\sigma) = (F(\sigma_{11} - \sigma_{22})^2 + G(\sigma_{22} - \sigma_{33})^2 + H(\sigma_{33} - \sigma_{11})^2 + 2L\sigma_{12}^2 + 2M\sigma_{23}^2 + 2N\sigma_{31}^2)^{1/2}. \quad (3)$$

\mathbf{S} is the deviatoric stress tensor, $n = 3.5$ is the power-law exponent, and \mathbf{A} is a rank-4

nondimensionalized anisotropic fluidity tensor reduced to a 6×6 matrix:

$$\mathbf{A} = \frac{2}{3} \begin{bmatrix} F+H & -F & -H & 0 & 0 & 0 \\ -F & G+F & -G & 0 & 0 & 0 \\ -H & -G & H+G & 0 & 0 & 0 \\ 0 & 0 & 0 & L & 0 & 0 \\ 0 & 0 & 0 & 0 & M & 0 \\ 0 & 0 & 0 & 0 & 0 & N \end{bmatrix}. \quad (4)$$

Finally, with the best-fit Hill coefficients, we compute the fluidity tensor from (4) and predict a new strain rate using the stress tensor obtained from the geodynamic models in ASPECT. This representation of AV has yet to be implemented into the geodynamic model, and with MDM+AV here we only look at how much AV changes the texture prediction part of the model. It is also important to note that the calculation of the anisotropic fluidity tensor was performed in the LPO reference frame and subsequently, we back-rotated the fluidity tensor to the model reference frame (Supporting Information).

2.4 Model Setup

2.4.1 Shear Box Model

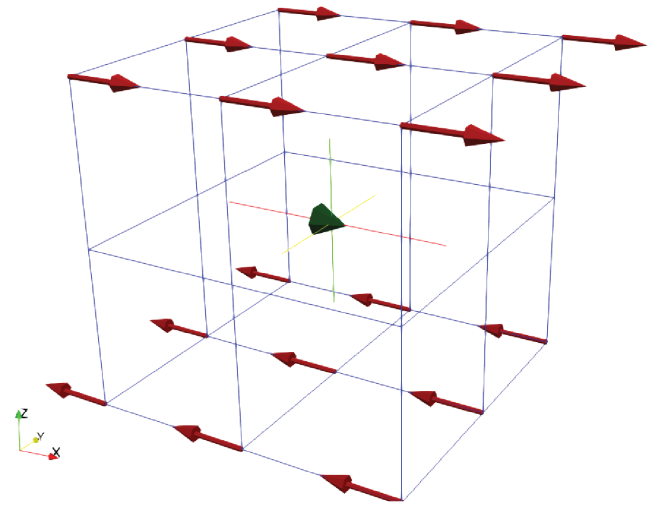


Figure 1 – Shear box model set-up and velocity boundary conditions. One particle with 5000 olivine grains sits in the center of the box to track the texture evolution.

The shear box is defined as a $1 \times 1 \times 1 \text{ m}^3$ cube in ASPECT, with one particle consisting of 5000 olivine grains positioned at the center of the box, corresponding to the coordinate (0,0,0) (Figure 1). We track the stress and strain states and look at the texture evolution of this particle. A constant velocity in the x-direction that is equal in magnitude to the z-coordinate (depth) is applied throughout the box, resulting in velocities of 0.5 m/s on the top and bottom faces of the box, pointing in opposite directions, shown as arrows in Figure 1. Consequently, the second invariant of the strain-rate tensor ($\dot{\epsilon}_{II}$) at the particle is 0.5 s^{-1} . The shear box is deformed for 20 seconds under this velocity, and the

total shear strain (henceforth referred to as strain) is thus 10. Subsequently, the applied strain rate and deformation tensors of the shear box are used as input for MDM and MDM+AV to calculate the texture evolution as defined above. The velocity gradient tensor is defined as follows:

$$D = \begin{bmatrix} 0 & 0 & 1 \\ 0 & 0 & 0 \\ 0 & 0 & 0 \end{bmatrix}. \quad (5)$$

2.4.2 Subduction Model

For the subduction model, we use the same settings as *Fraters and Billen (2021)* with a kinematically-driven subducting plate, and particles placed in particular locations to track the flow around the subducting plate. The domain is 2500×2000×800 km³ in the x-, y-, and z-directions, respectively and we use adaptive mesh refinement to have a larger resolution in the regions of interest, for example near the slab, resulting in a maximum cell size of 5x5x5 km and a minimum cell size of 0.625x0.625x0.625 km. Within the domain, an oceanic plate is pushed towards and subducted beneath a continental plate in the negative x-direction perpendicular to the plate boundary, with a dip angle of 50–55° and a constant velocity of 3 cm/yr to initiate and drive subduction from the back of the subducting plate (Figure 2). The subduction trench spans 1000 km and is located 500 km from both sides of the model domain. Vertically, the model consists of a wet crust (30 km), a dry lithosphere (up to 100 km), a wet upper mantle (up to 660 km), and a lower mantle (660 to 800 km) (Figure 2). The model includes two weak zones with an angle of internal friction of 5° and a cohesion of 1×10⁴ Pa, which is weaker than the surrounding lithosphere. The model employs free-slip boundary conditions for its top, open boundary conditions for the four vertical side surfaces beneath 100 km depth, and no-slip boundary conditions for the bottom. A velocity boundary condition is defined for the lithospheric layer extending down to 100 km.

We use incompressible viscoplastic rheology for the subduction model, and the viscosity is thus defined as:

$$\eta = \frac{1}{2} A^{-\frac{1}{n}} d^{\frac{m}{n}} \dot{\epsilon}_{II}^{\frac{1-n}{n}} \exp\left(\frac{E + PV}{nRT}\right), \quad (6)$$

where A is the prefactor, n is the stress exponent, d is the grain size, m is the grain-size exponent, $\dot{\epsilon}_{II}$ is the square root of the second invariant of deviatoric strain rate, E is the activation energy, P is the pressure, V is the activation volume, R is the gas exponent, and T is the temperature. Since dislocation creep is expected to dominate upper mantle deformation and diffusion creep in the lower mantle, we allow both dislocation creep and diffusion creep in our model, thus, the composite viscosity is defined as $\frac{\eta_{diff} \times \eta_{dist}}{\eta_{diff} + \eta_{dist}}$. The values we use for the

rheological behavior in the subduction model can be found in the Supporting Information, and the parameter files are shared in Zenodo (*Wang, 2023*). For the rheological behavior we described above using Eq. 5, the viscosity in the upper mantle is pressure-dependent and will increase as the depth increases (Figure 2).

We place 75 particles around the slab to study mantle flow on all sides of the slab and observe the deformation and texture tracked by these particles. Most particles are located on the plane perpendicular to the y-axis at the center of the subducting plate in the sub-slab region and the mantle wedge region (the region right behind and in front of the subducting slab, respectively). In the results section, we examine two representative particles that have enough deformation that the anisotropy is strong enough for analysis to demonstrate the spatial differences in deformation history for particles around a subduction zone. One particle is from the sub-slab area and the other one is from the mantle wedge area.

For the MDM and MDM+AV texture simulations, we use the temperature, strain rate, velocity gradient, and stress that the particle experienced during the model run in ASPECT. In ASPECT, the subduction model has a composite rheological behavior with both dislocation creep and diffusion creep as mentioned above, while in the MDM+AV model, we assume that only dislocation creep gives rise to AV. We compute an effective viscosity $\eta_{effective} = \frac{\sigma}{\dot{\epsilon}}$ for the MDM+AV model using the second invariants of the stress tensor (σ) from ASPECT and strain rate tensor ($\dot{\epsilon}$) predicted using MDM+AV and eq. 1. To compare the change in viscosity under deformation with and without the effect of AV, we also compute a predicted strain rate using the stress from ASPECT assuming an isotropic texture and an effective viscosity that we call isotropic viscosity (IV) for this strain rate.

We compare the development of textures both quantitatively and qualitatively using texture scores representing the strength and shape of textures and pole figures of the distribution of the olivine a-axis representing the orientation of textures. The misorientation index (M-index) is defined as the difference between the observed misorientation angles and the misorientation angles for a uniform texture (*Skemer et al., 2005*). A minimum M-index score of 0 represents a uniform texture, and a maximum M-index score of 1 represents a strong single-crystal texture. To evaluate the shape of textures, we utilize the pointiness, girdle-ness, and randomness scores (P, G, and R scores) (*Vollmer, 1990*). They represent components of a particular crystallographic axis distribution derived from the eigenvalues of the orientation tensor for a single crystallographic axis. A high P, G, or R score corresponds to a point-like (single crystal orientation) shape, a girdle-like single-plane shape, or a uniform

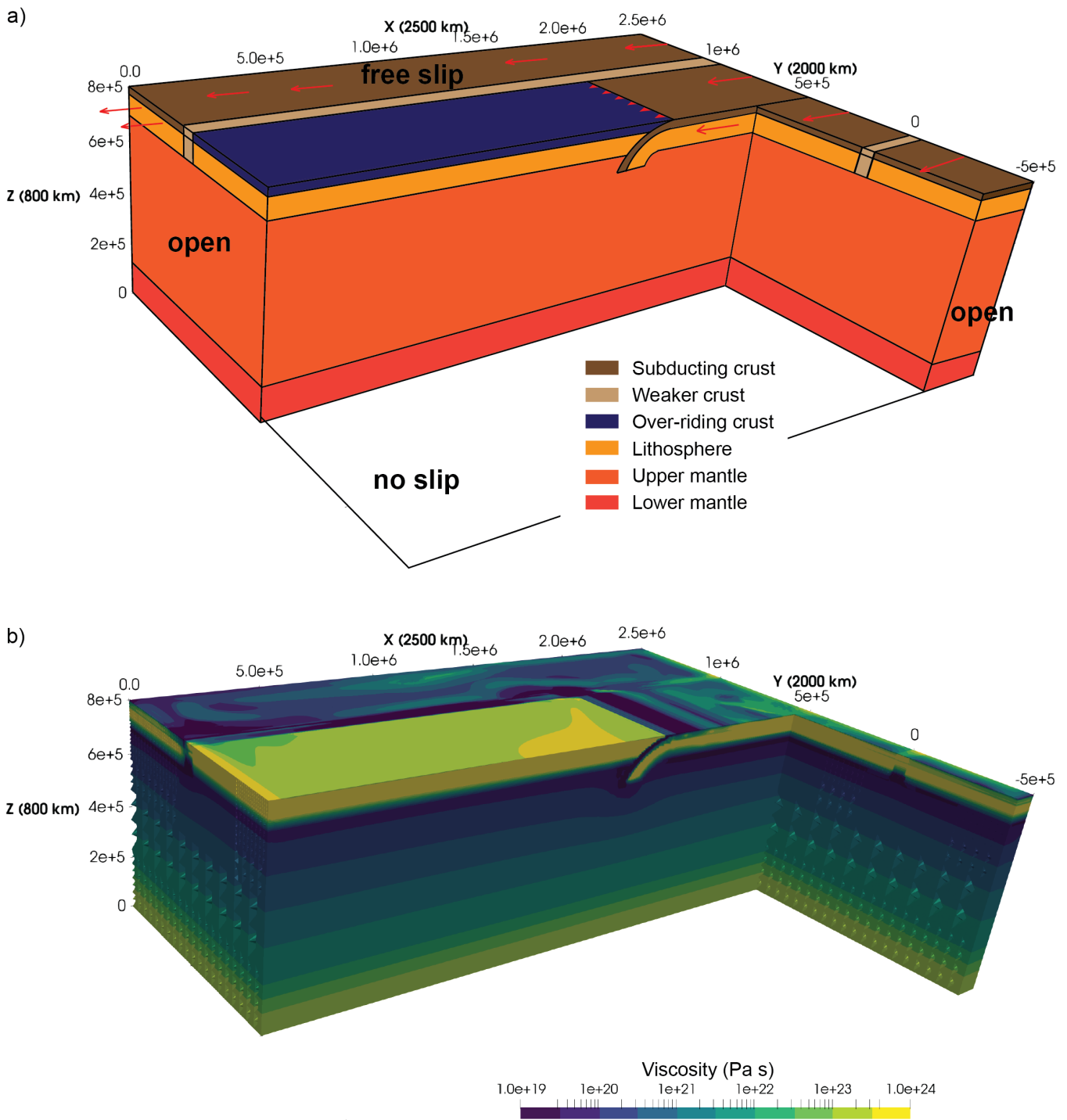


Figure 2 – Initial setup of the subduction model, showing **a)** the materials and boundary conditions; **b)** viscosity.

texture, respectively. The P, G, and R scores add up to 1 and can be plotted on a ternary diagram.

3 Results

3.1 Shear Box

The particle undergoes a simple deformation path in the shear box setup with a constant strain rate and stress. In all three texture models, the particle starts with an isotropic texture and gradually reorients the a-axis direction into the shear direction as deformation accumulates. The girdle-ness score of

the textures reaches its peak around an accumulated strain ($\epsilon_{ii}^n = \epsilon_{ii}^{n-1} + dt\dot{\epsilon}_{ii}$, where n is the time step and $\dot{\epsilon}_{ii}$ is the second invariant of strain rate) of 1 and starts decreasing, while the randomness score ($R = 1 - P - G$) decreases from the initial value of ~1 to less than 0.2 at an accumulated strain of 2 (Figure 3).

When comparing the texture evolution models, the alignment of the olivine a-axis with the shear direction in the D-Rex model occurs at a lower strain compared to the MDM and MDM+AV models. This distinction becomes visually evident in the pole figures (Figure 3a). The pointiness of a-axes and M-index scores exhibit a more rapid increase with

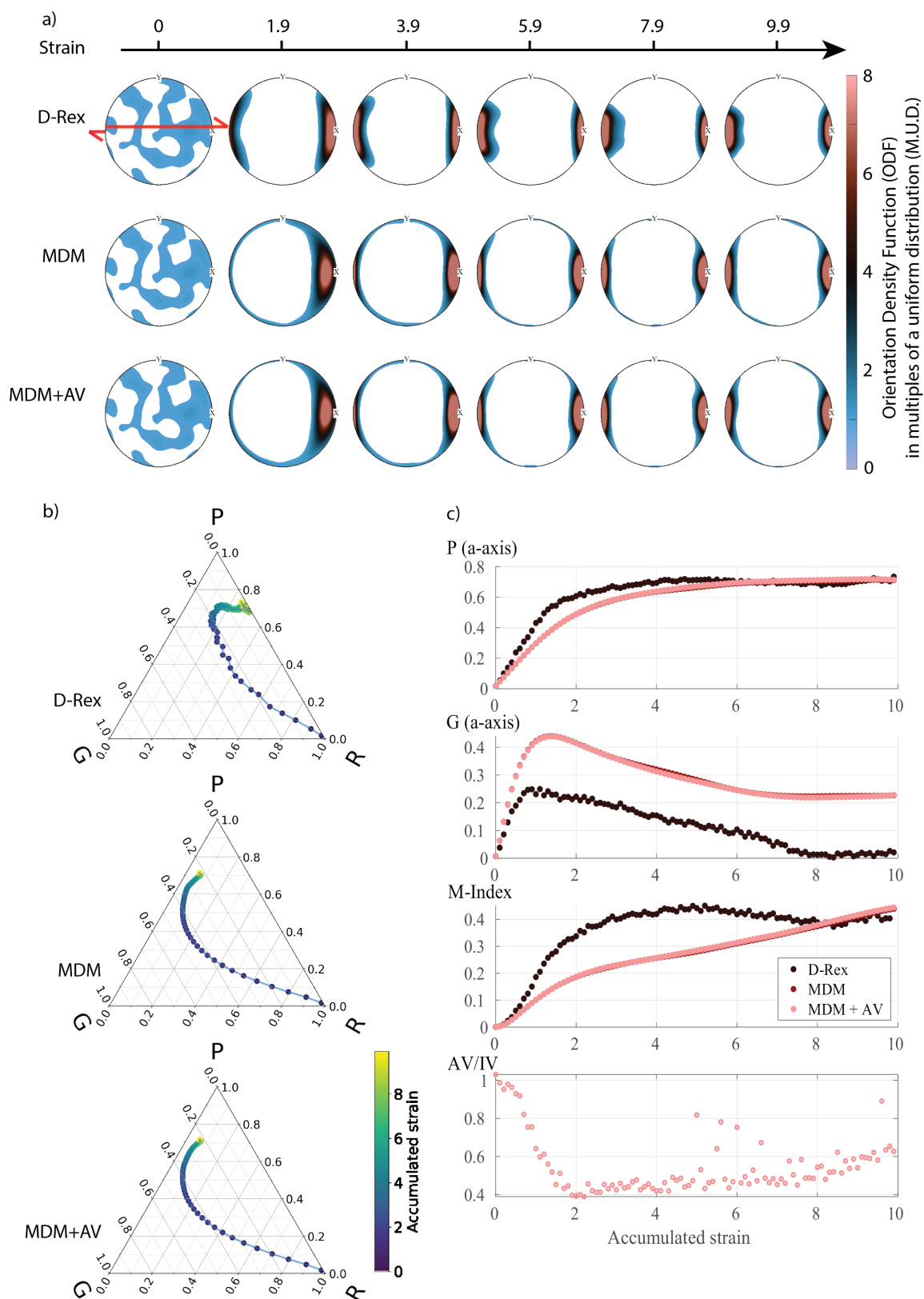


Figure 3 – a) Pole figures (upper hemisphere) illustrating the olivine particle’s a-axis [100] orientation in the shear box at different accumulated strains in the shear box model. Pole figures are contoured based on multiples of uniform distribution. The x and y directions are the same as in Figure 1. **b)** Ternary diagram plotting the pointiness, girdle-ness, and randomness (P, G, R) scores of the olivine a-axis texture. The evolution of P, G, and R scores is colored by accumulated strain. **c)** Texture scores (pointiness, girdle-ness, and M-index) of the olivine particle in the shear box, as predicted by different methods (colored dots) and the ratio of effective viscosity from the anisotropic MDM+AV model (AV) relative to an isotropic viscosity (IV) assumption, as a function of accumulated strain.

increasing accumulated strain for D-Rex textures, in contrast with the MDM and MDM+AV textures

(Figure 3b and c). During the early stage of deformation before accumulated strain reaches

~1, the texture predicted by MDM and MDM+AV tends to organize into a girdle-like pattern. Then the girdle-ness score begins to decrease, and the pointiness score gradually catches up with the texture predicted by D-Rex. The girdled pattern in the textures predicted by MDM and MDM+AV persists until the end of the model, with a girdle-ness score of 0.23, in contrast to D-Rex, which shows no girdled pattern at the end (final girdle-ness score of 0.02). This difference could be important for viscous anisotropy because the girdle in MDM-based models will result in more grains in favorable or unfavorable orientations as compared to D-Rex, potentially modifying the deformation rate. At an accumulated strain of 5, the M-index from D-Rex reaches its peak around 0.45 but starts to decrease and fluctuate (0.41 ± 0.02) after that. In contrast, the M-index scores for both MDM and MDM+AV continue to increase monotonically, surpassing the M-index score for D-Rex after an accumulated strain of 8. Eventually, the textures predicted by all three methods converge with a dominant point-like pattern and comparable pointiness scores (D-Rex: 0.734, MDM: 0.712, MDM+AV: 0.715) and M-index scores (D-Rex: 0.440, MDM: 0.439, MDM+AV: 0.445). Adding the AV component does not significantly change the texture predicted by MDM+AV because the texture is already well-oriented for the applied deformation, and it only increases the final M-index by less than 1% compared to D-Rex and MDM. When we examine the effective viscosity calculated from the equivalent stress and strain rate ($\eta = \frac{\sigma}{\dot{\epsilon}}$) using the MDM+AV method, we find that this more aligned olivine texture reduces the effective viscosity by 60% up to an accumulated strain of 2 relative to the initial time step where the model is isotropic (Figure 3c). This agrees with the results by Király *et al.* (2020).

3.2 Subduction

Building upon our analysis of shear-box textures discussed earlier, we compare the texture predictions using similar criteria in a subduction setting. Figure 4 illustrates a sequence of snapshots of a cross-section along the x-direction in the middle of the subduction zone model. The snapshots are captured at 10-Myr intervals and show the viscosity (left) and strain rate (right) fields. Velocity vectors (white arrows) are displayed, in which the paths of analyzed particles are highlighted as blue and pink lines. The mantle wedge corner flow and the poloidal flow resulting from the slab's roll-forward motion are made evident by the velocity vectors (Figure 4). As subduction progresses, our trench gradually moves forward and has advanced approximately 100 km by the end of the model at 40 Myr (Figure 4e). Our analysis focuses on two particles representing distinct regions in a subduction zone: the sub-slab region (blue) and the mantle wedge region (pink). These particles experience different mantle flow patterns as the slab continues to subduct. The particle in the sub-slab region is located about 50 to

100 km beneath the lithosphere, moving with the mantle flow behind the subducting slab forwards and downwards simultaneously. The particle in the mantle wedge follows the corner flow upwards and towards the slab until about 5 Myr. Then it approaches the slab with its temperature dropping from around 1535 K to below 1400 K and starts to move downwards together with the slab. In general, the particles we put in the sub-slab region experience less deformation than particles in the mantle wedge region; the accumulated strain within the mantle wedge can be 4 times larger for the time and rheology imposed.

3.2.1 Sub-slab Region

For the less deformed sub-slab particle, our results show that around an accumulated strain of 1, D-Rex predicts a significantly different a-axis symmetry, where the a-axis points subparallel to the z-axis, while for MDM and MDM+AV the texture is roughly parallel to the x-axis (Figure 5a). Apart from this difference, both MDM and MDM+AV predict a similar texture evolution, characterized by a more girdle-like shape of the a-axis distribution compared to D-Rex's prediction, which transitions into a more point-like shape starting from a strain of 0.8 (Figure 5a). This behavior is consistent with the observation made in the shear-box experiment (Figure 3a). D-Rex predicts a shift from a point-like to a more random texture after an accumulated strain of 1, while both MDM and MDM+AV predict a steady increase in the pointiness score. Additionally, around an accumulated strain of 0.8, the girdle-ness of the texture from MDM+AV reaches its peak of 0.33 and then starts to decrease slowly, while the pointiness score continues to increase, becoming the highest among the three methods (Figure 5c). As the texture develops in this particle, the effective viscosity computed from MDM+AV (AV) becomes increasingly weaker than the effective viscosity for an isotropic texture (IV) (Figure 6c). The AV decreases to about 80% of the IV at an accumulated strain of ~0.65 as a girdle plane is forming in the texture (Figure 5c). Then, as the point-like shape gains dominance in the texture, the AV-to-IV ratio remains stable until the pointiness score approaches the girdle-ness score, eventually leading to a 30% weakening of the AV near the end of the model with an accumulated strain of ~1.4. To help understand the evolution of the effective viscosity for MDM+AV, we plot the orientations of the principal stresses from the deviatoric stress tensor derived from the subduction model in ASPECT above the texture plots (Figure 5a). A positive value corresponds to extension, while a negative stress is compressive. The significant increase in the magnitude of the largest principal stress (σ_1) coincides with the drop in the effective viscosity for both AV and IV at an accumulated strain of ~0.9 (Figure 6a and c), consistent with the shear-thinning nature of the power law in Eq. 1. The slight misalignment of σ_1 with the direction of

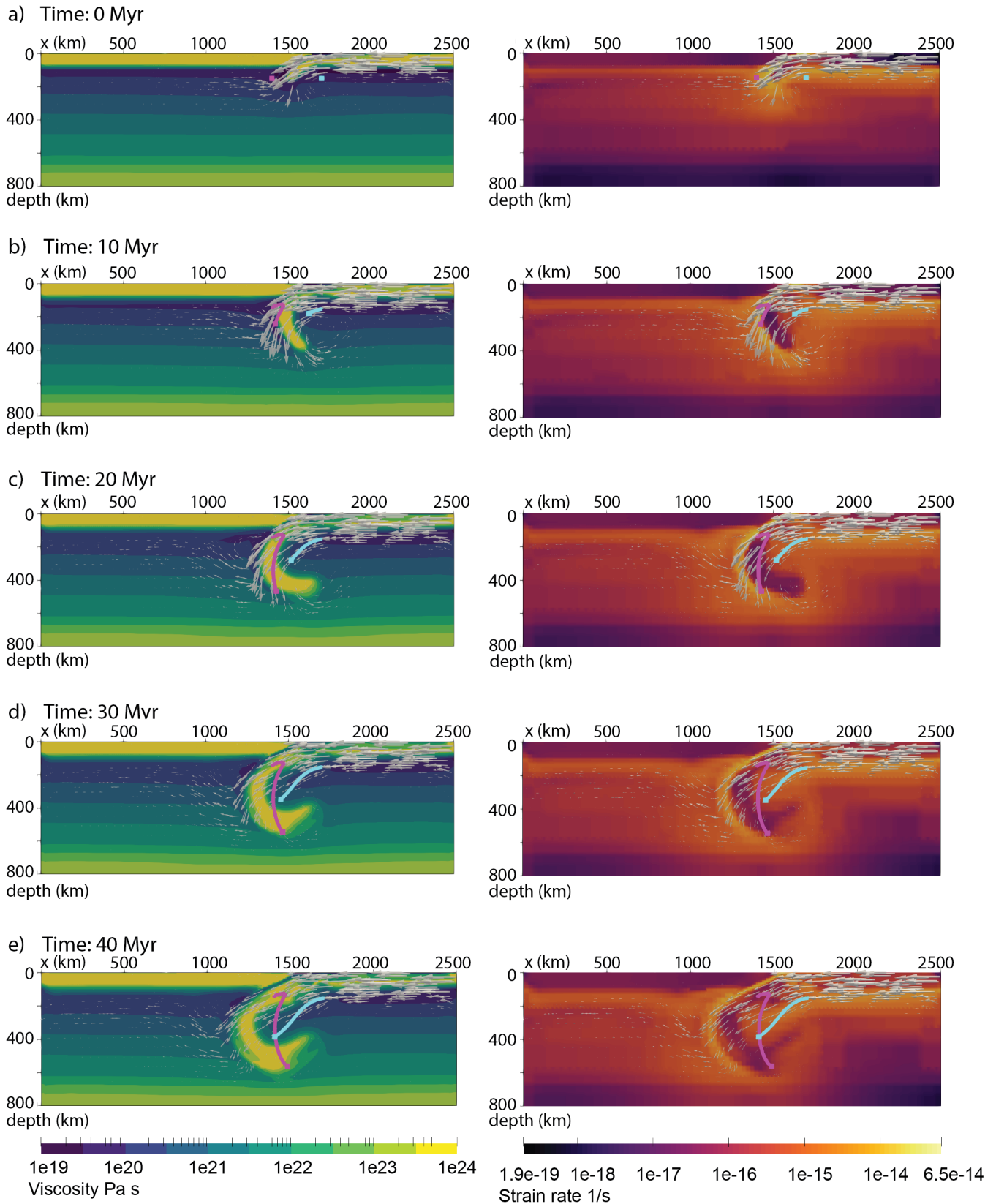


Figure 4 – Slice in the middle of the subduction model (ASPECT with texture model D-Rex), displaying the viscosity (left column) and strain rate (right column) represented by the background color, velocity represented by the white arrows above the background, and the two particles of interest represented by spheres (blue: sub-slab particle, pink: mantle-wedge particle). The movement of the particles is captured in five snapshots (0 Myr, 10 Myr, 20 Myr, 30 Myr, and 40 Myr) during the model. MDM and MDM+AV use the particle deformation paths from this model. The horizontal axis is the x-axis, and the vertical axis is the z-axis.

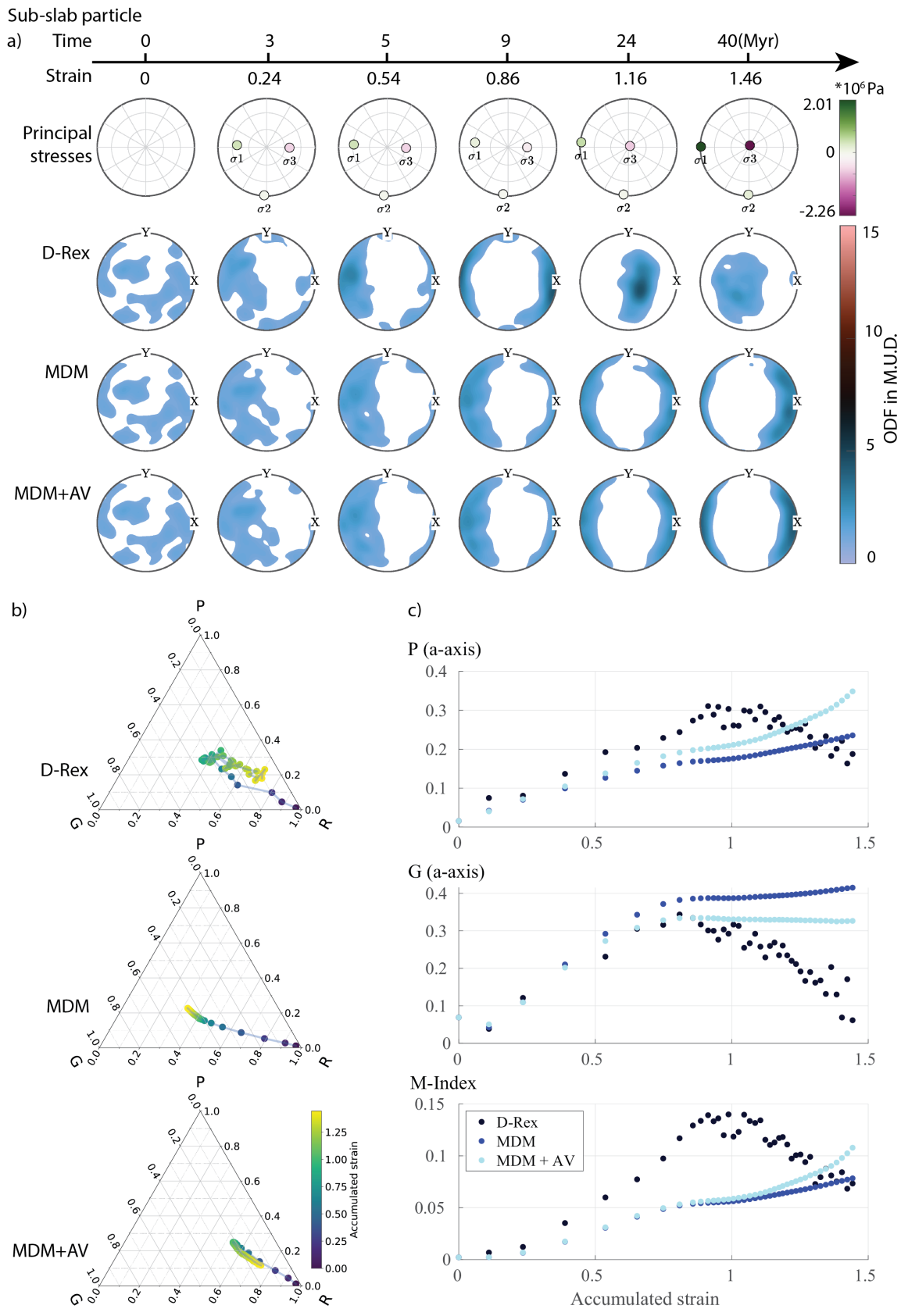


Figure 5 – a) Principal stresses of the deviatoric stress tensor and pole figures (upper hemisphere) of an olivine particle ([100] axis) from the sub-slab area of the subduction model at selected accumulated strains. The particle’s location can be found in Figure 4 (blue). The orientations of the x, y, and z-axes in these pole figures are the same as in Figures 2 and 4, so the xy-plane here is the horizontal plane in Figure 2 as viewed from the top of the model. The orientations of the principal stresses are also indicated for each selected strain. We follow the convention of positive tensional stress. **b)** Ternary diagram of the particle’s P, G, and R scores from the sub-slab area of the subduction model. **c)** Texture scores (P, G scores, and M-index) of the olivine particle from the sub-slab area of the subduction model.

the a-axis point maximum (about 10~20°) correlates with the weakening of AV relative to IV after an accumulated strain of ~0.9. This relative decrease in AV also correlates with the increasing pointiness score (Figures 5 and 6a). The total accumulated strain for this particle is around 1.5, and the texture predicted by all three methods has moderate strength, with a maximum M-index of 0.15.

3.2.2 Mantle Wedge Region

For the particle in the mantle wedge region, our analysis reveals that MDM+AV predicts a more point-like texture (MDM+AV pointiness score = 0.65), distinct from the strong girdle-like texture predicted by MDM (MDM girdle-ness score = 0.56) and the weaker point-like texture by D-Rex (D-Rex pointiness score = 0.45) (Figure 7). Still, D-Rex is the fastest to develop a point-like feature in the texture, while the MDM texture tends to organize into a girdle plane. In the MDM+AV model, the texture is similar to MDM until an accumulated strain of 5, at which point the point-like feature replaces the girdle-like feature, and, consequently, the pointiness score predicted by MDM+AV reaches the largest of all models at the end of the model. Initially, AV is weaker than IV during the formation of the girdle plane, on which the principal stress direction lies (Figures 6b, 6d, and 7a). As the principal stresses rotate away from the girdle plane in the texture, the AV of the particle is hardened to about 1.5 times the IV. Gradually, the a-axis maximum rotates to bisect σ_1 and σ_3 at a strain of ~4, associated with AV decreasing to about half of the IV ($AV/IV \approx 50\%$) (Figure 6d). Towards the end of the simulation, both σ_1 and σ_3 are aligned perpendicular to the developing point maximum within the texture, and the particle experiences a hardening effect of AV, reaching up to about twice of IV ($AV/IV \approx 200\%$) (Figures 6b, 6a).

4 Discussion

The findings presented in the results section provide valuable insights into the implications of different texture evolution models and the role of anisotropic viscosity (AV) within both simple shear and subduction systems. In the context of simple deformation settings, such as in a shear box model, our study reveals that the olivine texture predicted by the D-Rex method aligns more rapidly with the shear direction compared to the texture predicted by the MDM, consistent with previous modeling outcomes from *Hansen et al.* (2016a). Based on *Hansen et al.* (2016a) and *Boneh et al.* (2015), VPSC is similarly fast to develop a pointy texture, and with higher strains, VPSC predicts stronger textures (with larger pointiness score and m-index). As strain accumulates, textures predicted by D-Rex, MDM and MDM+AV reach similar pointiness and M-index scores, eventually aligning with the shear direction under large strain. The main distinction between the MDM and the D-Rex textures lies in

the girdle-ness scores. While the random texture starts to organize into a point-like shape in the D-Rex model, a girdle is forming in the MDM model, and the girdle-ness score for MDM remains larger than the girdle-ness score for the D-Rex model at the end of the experiment. The presence of a girdle shape in the texture predicted by MDM has also been observed by *Hansen et al.* (2016a).

In the shear box model, we observe an inverse correlation between the effective viscosity and the pointiness score of the olivine a-axis (Figure 3c); in other words, the lower the viscosity, the higher the pointiness score. As was demonstrated by *Király et al.* (2020), the effective viscosity decreases by about 60% as the pointiness of the texture increases in the model with AV, leading to a substantial amount of weakening. Overall, we find that adding AV does not change the texture significantly. This aligns with our expectation, given that the shear box model has a simple and homogeneous set-up, and the boundary conditions are imposed such that the variation in viscosity cannot change the imposed strain rate. The texture developed in the shear box model is already well-oriented for the applied deformation, while a strong unfavorably oriented texture, as we found in the subduction model, could be more significantly impacted by AV. If we incorporate MDM+AV into geodynamic modelling tools where AV can modify strain rate, the effect of AV can be amplified. Since D-Rex textures align to the shear direction faster and the effective viscosity anticorrelates with the pointiness score, we expect a stronger anisotropy and more weakening if we implement AV with D-Rex textures (as in ASPECT) in the shear box model.

By examining the particles from the sub-slab and mantle-wedge regions of a trench-advance subduction model, we observe distinct texture evolutions showing more differences among the MDM+AV, MDM, and D-Rex methods. The amount of deformation and strain rate differs across particles, with sub-slab particles experiencing less deformation (~1 accumulated strain) compared to mantle wedge particles (~6 accumulated strain) over 40 Myrs of simulation. This difference agrees with the roll-forward geometry and the mobility of the trench in our subduction model. The resulting texture strength correlates with the intensity of deformation (strain), where particles experiencing substantial deformation tend to have a stronger texture, characterized by higher texture scores. It is worth noting that the amount of deformation from the subduction model is not very large compared to most subduction zones on Earth, due to the limited lateral motion of the trench. With more rigorous mantle flow around the slab, we expect more deformation in a trench-retreating subduction model (*Di Giuseppe et al.*, 2008; *Schellart and Moresi*, 2013), and thus a larger effect of anisotropic viscosity. If the mantle has pre-existing textures (e.g., olivine particles deformed before they approach the subduction zone) resulting in an initial strong anisotropic

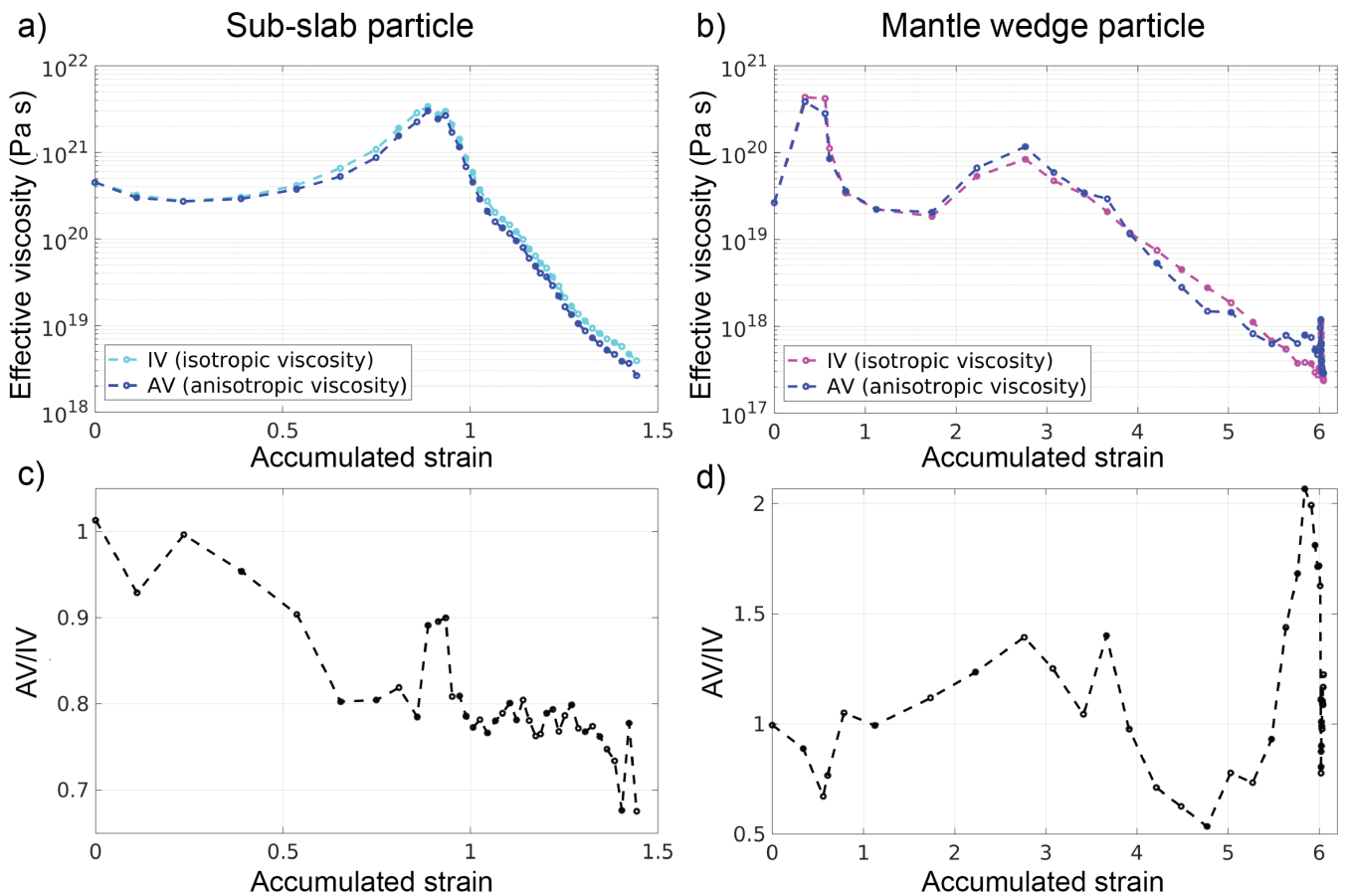


Figure 6 – Above: Effective viscosity assuming isotropic viscosity (IV) and for anisotropic viscosity (AV) calculated using MDM+AV for **(a)** the sub-slab particle and **(b)** the mantle wedge particle. Below: The ratio between AV and IV (AV/IV) for **(c)** the sub-slab particle and **(d)** the mantle wedge particle.

behavior, the difference between isotropic and anisotropic viscosity could also be larger (Hansen et al., 2016a; Mameri et al., 2023).

Although their amount of deformation is different, both particles we studied in the subduction model show girdle-like textures that are much stronger for MDM than for D-Rex, consistent with the observations from the shear box experiments. The pointiness of the D-Rex texture in the sub-slab particle is not significant at an accumulated strain of 1.5; however, on the other side of the slab in the same model the strain is much larger (~6) and the pointiness of the mantle wedge particle is around twice as large. Different from the shear box model, for particles in a subduction model, olivine textures predicted by D-Rex and MDM also exhibit differences in the mean direction after an accumulated strain of about 1 (Figures 5a, 7a). This could be a result of the emphasis on dynamic recrystallization in D-Rex or differences in parametrization between D-Rex and MDM. MDM+AV initially predicts a texture evolution trend similar to MDM for both particles. However, after an accumulated strain of ~5 in the mantle wedge, a point-like pattern starts to dominate the MDM+AV texture, similar to the texture predicted by D-Rex (Figure 7a). In addition, the inclusion of AV induces a rotation of the point maximum into

the y-direction, forming a texture that, if AV were implemented in the flow calculation, could change the particle path. This is due to the enhancement of the velocity gradient into the y-direction due to AV rheology. See part 3 of the Supporting Information.

The effect of AV may be reduced if we incorporate multiple deformation mechanisms acting together to accommodate the strain, especially when deformation mechanisms that do not generate LPO, such as diffusion creep, dominate. For both particles during the ASPECT model run, the dislocation creep mechanism dominates most of the modeled time ($\frac{\eta_{dislocation}}{\eta_{diffusion}} < 1$), where deformation by dislocation creep (with effective viscosity $\eta_{dislocation}$) is faster than deformation by diffusion creep ($\eta_{diffusion}$). This observation means that using a rheological model consisting only of power-law dislocation creep in MDM+AV remains a valid representation of the impact of AV.

By plotting the principal stress directions at different strain stages, we observe that both particles experience a significant increase in the principal stresses, especially the compressive stress σ_3 , as the sub-slab particle is pushed by the rolling slab, and the mantle wedge particle is pushed by the slab tip and the lower boundary. The weakening effect of AV, signaled by an AV-to-IV ratio smaller

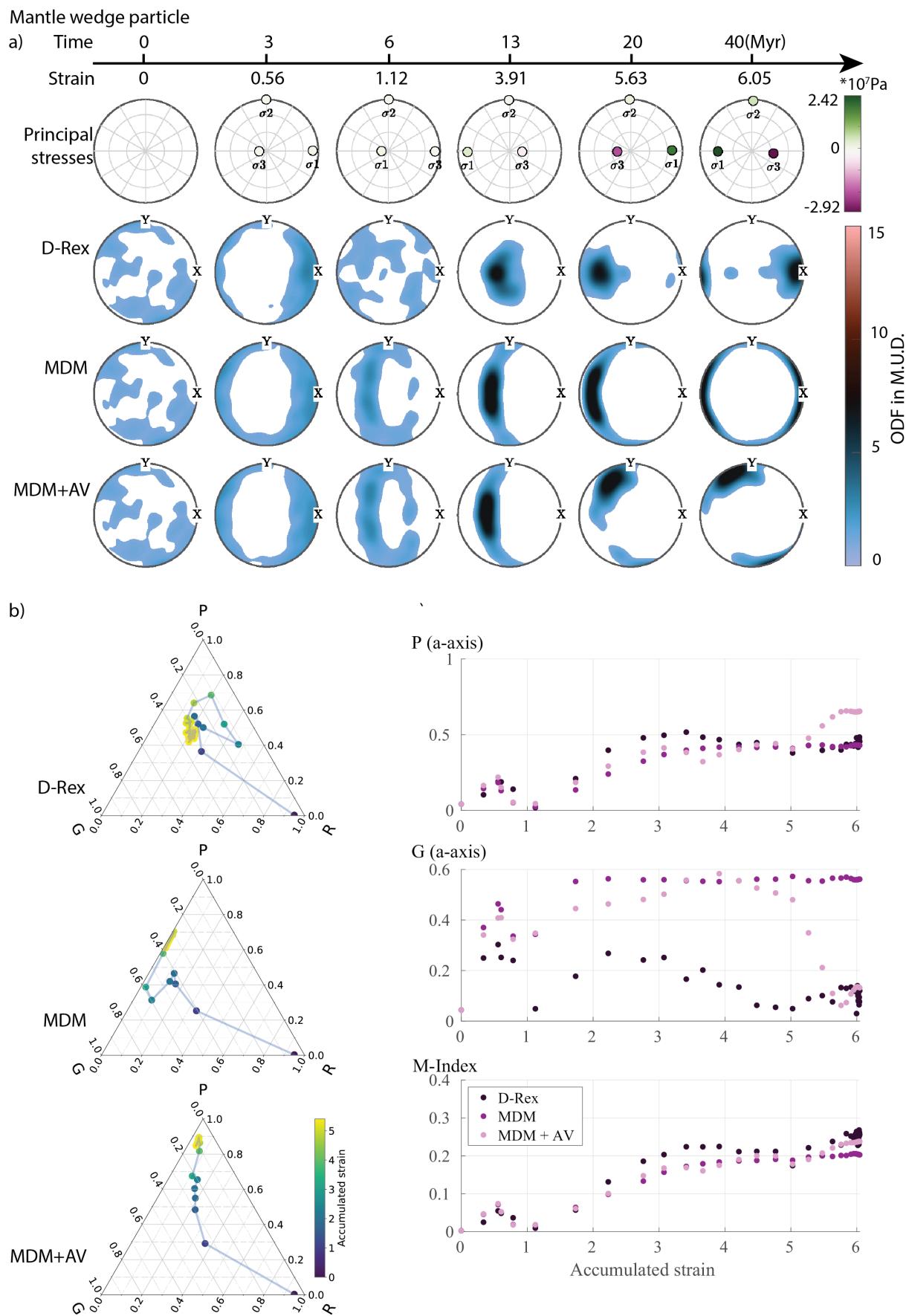


Figure 7 – a) Principal stresses of the deviatoric stress tensor and pole figures (upper hemisphere) of an olivine particle ([100] axis) from the mantle wedge area of the subduction model at selected accumulated strains. The particle’s location can be found in Figure 4 (pink). **b)** Ternary diagram of the P, G, and R scores of the olivine particle from the sub-slab area of the subduction model. **c)** Texture scores (P, G scores, and M-index) of the olivine particle from the sub-slab area of the subduction model.

than 1, tends to coincide with the maximum a-axis direction being at an angle to both σ_1 and σ_3 (Figures 5 and 7). The largest weakening effect occurs when the a-axis maximum bisects σ_1 and σ_3 , which is observed at a strain of ~ 4 for the mantle-wedge particle (Figure 7a). That is when the a-axis maximum is aligned with the direction of maximum shear stress. This observation is consistent with the maximum shear stress being well resolved on the two weakest slip systems, (010)[100] and (001)[100] and is supported by previous studies (Knoll et al., 2009; Mameri et al., 2023; Tommasi and Vauchez, 2001). For the sub-slab particle, the MDM+AV effective viscosity is smaller than the isotropic viscosity throughout the model run, and AV could be weakened to about 70% of IV. The effect of AV is larger and more complex for the particle in the mantle wedge region, which experiences both weakening ($\frac{AV}{IV} \sim 50\%$) and hardening ($\frac{AV}{IV} \sim 200\%$) effects of AV depending on the relationship between the texture and the stress conditions. This is because the accumulated strain in the mantle wedge is larger, leading to a stronger texture and anisotropy, while the stress on the particle is changing. Such a weakening or hardening effect would modify the deformation path of the particle and the mantle flow patterns for a subduction setting. It is important to notice that the $\frac{AV}{IV}$ ratio is not a smooth curve as the accumulated strain increases. This reflects both the uncertainty in finding Hill's parameters for computing the anisotropic viscosity tensor using the best-fit method and the changing relationship between the principal stress directions and the texture.

To fully comprehend the effect of AV in a subduction zone, it will be necessary to implement AV rheology into a geodynamic modeling software like ASPECT, which would allow us to study the modified mantle deformation. Linking the AV component to the texture prediction module (D-Rex) in ASPECT might produce different results compared to MDM+AV. Although the textures predicted by D-Rex and MDM can be similar in strength and orientation under simple deformation, as in a shear box setting (Figure 3a), they can vary significantly in the subduction model (Figures 5a and 7a). For the sub-slab particle in the subduction model, the mean a-axis orientation predicted by D-Rex is more point-like and in a direction perpendicular to the girdle-like texture predicted by MDM and MDM+AV (Figure 5a). However, the texture predicted by MDM+AV on the particle in the mantle wedge region deviates from the girdled pattern predicted by MDM and is dominated by a point-like pattern (Figure 7a). These differences in texture prediction between MDM-based methods and D-Rex are expected since D-Rex accounts for the effect of water in activating different olivine fabric types, which could play a significant role in subduction systems. This could indicate that the inclusion of AV within a geodynamic model could affect olivine textures (and thus AV) more significantly than the method for modelling

texture evolution.

Our study uses an application of MDM+AV to quantify the effect of AV in both simple and complex scenarios. Based on this, we build a solid foundation for incorporating AV into numerical methods where AV associated with existing textures can modify the strain rates that are used to predict new textures. If the shear direction is the same as the texture alignment, the deformation needed to produce textures interpreted from seismic anisotropy is smaller with the effect of AV than for an isotropic material. However, the scope of this study is limited to textures tracked by a few particles within a specific subduction model. Further investigation should encompass different regions within a subduction zone to examine the spatial and temporal variations of the relationship between deformation and AV. Additionally, running models with diverse subduction settings, such as subduction with a retreating trench, oblique subduction, and flat subduction, will further enhance our understanding of the importance of AV and rock texture within subduction zones. To comprehensively explore this representation of AV, it is also crucial to run models that accurately represent specific subduction zones, compute seismic anisotropy, and compare the results with observations.

5 Conclusion

Our study explores olivine texture evolution in both simple shear box and subduction settings using three different methods, D-Rex, MDM, and MDM+AV, the last of which incorporates anisotropic viscosity into the texture development. The results are consistent with previous modeling and experimental results and show that the D-Rex texture is usually stronger and has a more point-like shape while the MDM texture develops more slowly and has a more girdle-like shape. The strain evolution of MDM+AV texture is similar to that of MDM texture, but anisotropic viscosity weakens the material by about 60% in the shear box model. For the subduction model, AV can both weaken and harden different regions in the subduction model, depending on the deformation path. Furthermore, because AV affects texture formation, incorporating AV into subduction models may significantly improve our interpretations of seismic anisotropy observations. In the future our aim is to implement AV within the ASPECT finite element code, where anisotropic viscosity would be (initially) coupled with textures determined by D-REX. Since D-Rex predicts a stronger and more point-like texture alignment, this implementation could lead to an overprediction of the weakening effect of AV with respect to simple models using MDM+AV (e.g., Király et al., 2020) for textures in which the LPO aligns with the main shear direction. Our results suggest that the AV of olivine greatly impacts texture formation, and the associated anisotropic rheology, in the upper mantle. Hence AV could significantly

affect geodynamic processes such as subduction, especially in the upper mantle where deformation by dislocation creep dominates.

Acknowledgements

This research was supported by the Research Council of Norway's project 314742 (ANIMA) and its Centers of Excellence projects 223272 (CEED) and 332523 (PHAB). The computational resource is provided by the Norwegian Research Infrastructure Service (NRIS/Sigma2) via projects NN9283k and NN9894k. We thank the Computational Infrastructure for Geodynamics (geodynamics.org) which is funded by the National Science Foundation under awards EAR-0949446 and EAR-1550901 for supporting the development of ASPECT. We thank the Journal Editor C. Magee, the Section Editor M. Arnould, the reviewers L. Mameri and N. Ribe for providing valuable advice for this article.

Author contributions

Y. Wang wrote the original draft, conducted analysis, and made figures under the supervision of **Á. Király** and **C. P. Conrad**. **L. Hansen** provided the original MDM method, and **M. Fraters** provided the original model parameter file. All authors contributed to the reviewing and editing of this article.

Data availability

The version of modeling software ASPECT used in this project is based on ASPECT 2.2.0 (Bangerth et al., 2020) and the CPO implementation from Fraters and Billen (2021) with additional changes not merged to the main repository. It is available through GitHub (github.com/Wang-yijun/aspect/tree/LPO_ss_tensor) and zenodo (Bangerth et al., 2023). Predictions of MDM and MDM+AV textures, comparisons of the textures, and analysis are generated with MATLAB and Python scripts available through Zenodo (Wang, 2023).

Competing interests

The authors declare no competing interests.

Peer review

This publication was peer-reviewed by Lucan Mameri and Neil Ribe. The full peer-review report can be found here: tektonika.online/index.php/home/article/view/67/87

Copyright notice

© Author(s) 2024. This article is distributed under the Creative Commons Attribution 4.0 International License, which permits unrestricted use, distribution, and reproduction in any medium, provided the

original author(s) and source are credited, and any changes made are indicated.

References

- Bangerth, W., J. Dannberg, R. Gassmoeller, and T. Heister (2020), ASPECT v2.2.0, doi: 10.5281/zenodo.3924604.
- Bangerth, W., J. Dannberg, M. Fraters, R. Gassmoeller, A. Glerum, T. Heister, R. Myhill, and J. Naliboff (2023), Wang-yijun/aspect: ASPECT for manuscript1, doi: 10.5281/zenodo.8219018.
- Blackman, D. K., D. E. Boyce, O. Castelnaud, P. R. Dawson, and G. Laske (2017), Effects of crystal preferred orientation on upper-mantle flow near plate boundaries: rheologic feedbacks and seismic anisotropy, *Geophysical Journal International*, 210(3), 1481–1493, doi: 10.1093/gji/ggx251.
- Boneh, Y., and P. Skemer (2014), The effect of deformation history on the evolution of olivine CPO, *Earth and planetary science letters*, 406, 213–222, doi: 10.1016/j.epsl.2014.09.018.
- Boneh, Y., L. F. G. Morales, E. Kaminski, and P. Skemer (2015), Modeling olivine CPO evolution with complex deformation histories: Implications for the interpretation of seismic anisotropy in the mantle, *Geochemistry, Geophysics, Geosystems*, 16(10), 3436–3455, doi: 10.1002/2015GC005964.
- Christensen, U. R. (1987), Some geodynamical effects of anisotropic viscosity, *Geophysical Journal International*, 91(3), 711–736, doi: 10.1111/j.1365-246X.1987.tb01666.x.
- Di Giuseppe, E., J. van Hunen, F. Funiciello, C. Faccenna, and D. Giardini (2008), Slab stiffness control of trench motion: Insights from numerical models, *Geochemistry, Geophysics, Geosystems*, 9(2), doi: 10.1029/2007GC001776.
- Falus, G., A. Tommasi, and V. Soustelle (2011), The effect of dynamic recrystallization on olivine crystal preferred orientations in mantle xenoliths deformed under varied stress conditions, *Journal of Structural Geology*, 33(11), 1528–1540, doi: 10.1016/j.jsg.2011.09.010.
- Fraters, M. (2020), The geodynamic world builder, doi: 10.5281/zenodo.3900603.
- Fraters, M., C. Thieulot, A. van den Berg, and W. Spakman (2019), The geodynamic world builder: a solution for complex initial conditions in numerical modeling, *Solid earth*, 10(5), 1785–1807, doi: 10.5194/se-10-1785-2019.
- Fraters, M. R. T., and M. I. Billen (2021), On the implementation and usability of crystal preferred orientation evolution in geodynamic modeling, *Geochemistry, Geophysics, Geosystems*, 22(10), doi: 10.1029/2021gc009846.
- Han, D., and J. Wahr (1997), An analysis of anisotropic mantle viscosity, and its possible effects on post-glacial rebound, *Physics of the Earth and Planetary Interiors*, 102(1), 33–50, doi: 10.1016/S0031-9201(96)03268-2.
- Hansen, L. N., M. E. Zimmerman, and D. L. Kohlstedt (2012), Laboratory measurements of the viscous anisotropy of olivine aggregates, *Nature*, 492(7429), 415–418, doi: 10.1038/nature11671.
- Hansen, L. N., Y.-H. Zhao, M. E. Zimmerman, and D. L. Kohlstedt (2014), Protracted fabric evolution in olivine: Implications for the relationship among

- strain, crystallographic fabric, and seismic anisotropy, *Earth and planetary science letters*, 387, 157–168, doi: 10.1016/j.epsl.2013.11.009.
- Hansen, L. N., J. M. Warren, M. E. Zimmerman, and D. L. Kohlstedt (2016a), Viscous anisotropy of textured olivine aggregates, part 1: Measurement of the magnitude and evolution of anisotropy, *Earth and planetary science letters*, 445, 92–103, doi: 10.1016/j.epsl.2016.04.008.
- Hansen, L. N., C. P. Conrad, Y. Boneh, P. Skemer, J. M. Warren, and D. L. Kohlstedt (2016b), Viscous anisotropy of textured olivine aggregates: 2. micromechanical model, *Journal of Geophysical Research, [Solid Earth]*, 121(10), 7137–7160, doi: 10.1002/2016JB013240.
- Hansen, L. N., M. Faccenda, and J. M. Warren (2021), A review of mechanisms generating seismic anisotropy in the upper mantle, *Physics of the Earth and Planetary Interiors*, 313, 106,662, doi: 10.1016/j.pepi.2021.106662.
- Heister, T., J. Dannberg, R. Gassmüller, and W. Bangerth (2017), High accuracy mantle convection simulation through modern numerical methods – II: realistic models and problems, *Geophysical Journal International*, 210(2), 833–851, doi: 10.1093/gji/ggx195.
- Hill, R. (1948), A theory of the yielding and plastic flow of anisotropic metals, *Proceedings of the Royal Society of London*, 193(1033), 281–297, doi: 10.1098/rspa.1948.0045.
- Kaminski, É., and N. M. Ribe (2001), A kinematic model for recrystallization and texture development in olivine polycrystals, *Earth and planetary science letters*, 189(3), 253–267, doi: 10.1016/S0012-821X(01)00356-9.
- Kaminski, É., N. M. Ribe, and J. T. Browaeys (2004), D-Rex, a program for calculation of seismic anisotropy due to crystal lattice preferred orientation in the convective upper mantle, *Geophysical Journal International*, 158(2), 744–752, doi: 10.1111/j.1365-246X.2004.02308.x.
- Karato, S.-I., H. Jung, I. Katayama, and P. Skemer (2008), Geodynamic significance of seismic anisotropy of the upper mantle: New insights from laboratory studies, *Annual review of earth and planetary sciences*, 36(Volume 36, 2008), 59–95, doi: 10.1146/annurev.earth.36.031207.124120.
- Király, Á., C. P. Conrad, and L. N. Hansen (2020), Evolving viscous anisotropy in the upper mantle and its geodynamic implications, *Geochemistry, Geophysics, Geosystems*, 21(10), doi: 10.1029/2020gc009159.
- Knoll, M., A. Tommasi, R. Logé, and J. Signorelli (2009), A multiscale approach to model the anisotropic deformation of lithospheric plates, *Geochemistry: Exploration, Environment, Analysis*, 10, doi: 10.1029/2009GC002423.
- Kronbichler, M., T. Heister, and W. Bangerth (2012), High accuracy mantle convection simulation through modern numerical methods, *Geophysical Journal International*, 191(1), 12–29, doi: 10.1111/j.1365-246X.2012.05609.x.
- Lee, K.-H., Z. Jiang, and S.-I. Karato (2002), A scanning electron microscope study of the effects of dynamic recrystallization on lattice preferred orientation in olivine, *Tectonophysics*, 351(4), 331–341, doi: 10.1016/S0040-1951(02)00250-0.
- Lev, E., and B. H. Hager (2008), Rayleigh–Taylor instabilities with anisotropic lithospheric viscosity, *Geophysical Journal International*, 173(3), 806–814, doi: 10.1111/j.1365-246X.2008.03731.x.
- Lev, E., and B. H. Hager (2011), Anisotropic viscosity changes subduction zone thermal structure: ANISOTROPIC VISCOSITY CHANGES WEDGE THERMAL STRUCTURE, *Geochemistry, Geophysics, Geosystems*, 12(4), doi: 10.1029/2010GC003382.
- Long, M. D., and T. W. Becker (2010), Mantle dynamics and seismic anisotropy, *Earth and planetary science letters*, 297(3), 341–354, doi: 10.1016/j.epsl.2010.06.036.
- Long, M. D., and P. G. Silver (2009), Shear wave splitting and mantle anisotropy: Measurements, interpretations, and new directions, *Surveys in Geophysics*, 30(4), 407–461, doi: 10.1007/s10712-009-9075-1.
- Lopez-Sanchez, M. A., A. Tommasi, W. B. Ismail, and F. Barou (2021), Dynamic recrystallization by subgrain rotation in olivine revealed by electron backscatter diffraction, *Tectonophysics*, 815, 228,916, doi: 10.1016/j.tecto.2021.228916.
- Mameri, L., A. Tommasi, J. Signorelli, and L. N. Hansen (2019), Predicting viscoplastic anisotropy in the upper mantle: a comparison between experiments and polycrystal plasticity models, *Physics of the Earth and Planetary Interiors*, 286, 69–80, doi: 10.1016/j.pepi.2018.11.002.
- Mameri, L., A. Tommasi, J. Signorelli, and R. Hassani (2020), Olivine-induced viscous anisotropy in fossil strike-slip mantle shear zones and associated strain localization in the crust, *Geophysical Journal International*, 224(1), 608–625, doi: 10.1093/gji/ggaa400.
- Mameri, L., A. Tommasi, A. Vauchez, J. Signorelli, and R. Hassani (2023), Structural inheritance controlled by olivine viscous anisotropy in fossil mantle shear zones with different past kinematics, *Tectonophysics*, 863, 229,982, doi: 10.1016/j.tecto.2023.229982.
- McKenzie, D. (1979), Finite deformation during fluid flow, *Geophysical Journal International*, 58(3), 689–715, doi: 10.1111/j.1365-246X.1979.tb04803.x.
- Molinari, A., G. R. Canova, and S. Ahzi (1987), A self consistent approach of the large deformation polycrystal viscoplasticity, *Acta Metallurgica*, 35(12), 2983–2994, doi: 10.1016/0001-6160(87)90297-5.
- Mühlhaus, H.-B., L. Moresi, B. Hobbs, and F. Dufour (2002), Large amplitude folding in finely layered viscoelastic rock structures, *Pure and Applied Geophysics*, 159(10), 2311–2333, doi: 10.1007/s00024-002-8737-4.
- Ribe, N. M., and Y. Yu (1991), A theory for plastic deformation and textural evolution of olivine polycrystals, *Journal of geophysical research*, 96(B5), 8325, doi: 10.1029/90jb02721.
- Sarma, G. B., and P. R. Dawson (1996), Effects of interactions among crystals on the inhomogeneous deformations of polycrystals, *Acta materialia*, 44(5), 1937–1953, doi: 10.1016/1359-6454(95)00309-6.
- Schellart, W. P., and L. Moresi (2013), A new driving mechanism for backarc extension and backarc shortening through slab sinking induced toroidal and poloidal mantle flow: Results from dynamic subduction models with an overriding plate, *Journal of Geophysical Research, [Solid Earth]*, 118(6), 3221–3248, doi: 10.1002/jgrb.50173.
- Signorelli, J., R. Hassani, A. Tommasi, and L. Mameri (2021), An effective parameterization of texture-induced viscous anisotropy in orthotropic materials with application for modeling geodynamical flows, *Journal of Theoretical, Computational and Applied Mechanics*, p. 6737, doi: 10.46298/jtcam.6737.

- Skemer, P., I. Katayama, Z. Jiang, and S.-I. Karato (2005), The misorientation index: Development of a new method for calculating the strength of lattice-preferred orientation, *Tectonophysics*, 411(1), 157–167, doi: 10.1016/j.tecto.2005.08.023.
- Tommasi, A., and A. Vauchez (2001), Continental rifting parallel to ancient collisional belts: an effect of the mechanical anisotropy of the lithospheric mantle, *Earth and planetary science letters*, 185(1), 199–210, doi: 10.1016/S0012-821X(00)00350-2.
- Tommasi, A., D. Mainprice, G. Canova, and Y. Chastel (2000), Viscoplastic self-consistent and equilibrium-based modeling of olivine lattice preferred orientations: Implications for the upper mantle seismic anisotropy, *Journal of geophysical research*, 105(B4), 7893–7908, doi: 10.1029/1999jb900411.
- Vollmer, F. W. (1990), An application of eigenvalue methods to structural domain analysis, *Geological Society of America bulletin*, 102(6), 786–791, doi: 10.1130/0016-7606(1990)102<0786:AAOEMT>2.3.CO;2.
- Wang, Y. (2023), Scripts to reproduce the results in manuscript1 (wang et al. 2023), doi: 10.5281/zenodo.8247969.